PR12-13-005

Measurement of $^{16}O(\gamma,\alpha)^{12}C$ with a bubble chamber and a bremsstrahlung beam

C. Ugalde *†

The University of Chicago, Chicago, IL 60637 and Argonne National Laboratory, Argonne IL 60439, USA

B. DiGiovine, R. J. Holt†, D. Henderson, K. E. Rehm

Argonne National Laboratory, Argonne IL 60439, USA

R. Suleiman †, A. Freyberger, J. Grames, R. Kazimi
M. Poelker, R. Mammei, D. Meekins, Y. Roblin

Jefferson Lab, Newport News, VA 23606, USA

A. Sonnenschein

Fermi National Accelerator Laboratory, Batavia, IL 60510, USA

A. Robinson

The University of Chicago, Chicago, IL 60637, USA

† Co-spokesperson

* Contact: Claudio Ugalde (cugalde@anl.gov)

5 May 2013

Abstract

We have devised a new technique for determining thermonuclear reaction rates of astrophysical importance. By measuring (γ,α) cross sections we will determine the (α,γ) reaction rate of ^{12}C(α,γ)^{16}O with a considerable improvement in sensitivity from previous experiments. Adopting ideas from dark matter search experiments with bubble detectors, we have found that a superheated liquid is sensitive to α-particle and heavy ion recoils produced from a γ ray beam impinging on the nuclei in the liquid. The main advantage of the new target-detector system is a density factor of 4-6 orders of magnitude higher than conventional gas targets. In addition, the inverse reaction (γ,α) has approximately 100 times the cross section of the (α,γ) reaction in this energy region. Also, the detector is virtually insensitive to the γ-ray beam itself, thus allowing us to detect only the products of the nuclear reaction of interest. This proposal requests 336 hours of beam time for measuring the ^{16}O(γ,α)^{12}C reaction.

Contents

1	Introduction	4
2	Method	8
3	Detector	13
4	Previous experiments	16
5	Backgrounds	21
6	Proposed experiment	24
6.1	Systematic errors	27
6.2	Beam time request and summary	29
References		31
7	Appendix A	33

1 Introduction

Thermonuclear burning in stars is responsible for the synthesis of most of the chemical elements heavier than helium in the universe. Over the years, both nuclear astrophysics theorists and experimentalists have struggled to understand the intricate paths along the table of nuclei followed by hydrostatic and explosive burning events. Today, at least it is clear that nucleosynthesis is a highly energy dependent process in which nuclei are produced from light to heavy as the increasingly strong Coulomb barrier needs to be overcome at higher and higher temperatures. The ascension flow is nevertheless far from being smooth. In some cases, narrow bottlenecks need to be surmounted in extreme conditions. In others, a single star may not be even able to reach certain regions of the nuclear chart.

Stars with a mass above 0.8 $M_\odot$ will evolve through core helium burning towards the end of their lifetime. This phase involves the formation of ^{12}C by the Salpeter process [1], in which three α-particles fuse sequentially in a two-step capture: first, two of them form the very unstable nucleus ^{8}Be, which in spite of its short lifetime, will be able to capture a third α-particle. This process occurs at conditions in which the stellar core is in an electron-degenerate state, so small temperature variations cannot be compensated by pressure changes. This makes the temperature rise very quickly to 0.12 billion K and as the Salpeter process has a rate with a very steep temperature dependence, the burning becomes violent and the helium core is ignited. The triple α-particle reaction proceeds through the $J^\pi=0^+$, E_x=7.65 MeV excited state in ^{12}C [2], the so called "Hoyle" state. At slightly higher temperatures, the ^{12}C(α,γ)^{16}O reaction is activated and both processes compete with each other in setting the abundance of carbon in the stellar core. Further α-particle capture processes at these burning temperatures are blocked by the ^{16}O(α,γ)^{20}Ne reaction, which is suppressed because of parity conservation rules. Therefore, the ^{12}C(α,γ)^{16}O nuclear reaction is resposible for defining the ratio of carbon to oxygen (two of the most important constituents of organic matter and life) in the stellar cores, and as a result, in the universe.

The abundance of most of the chemical elements is also affected by the ^{12}C(α,γ)^{16}O reaction in one way or another. For example, such is the case of the α nuclei, which are some of the most common species in the universe after hydrogen and helium. These nuclei belong to the chain of even-even nuclei with the same number of protons and neutrons ranging from ^{16}O up to ^{56}Ni, which is unstable and decays to form the abundant ^{56}Fe. Neutron capture elements ranging between iron and zirconium (weak s-process elements) are also affected by the ^{12}C(α,γ)^{16}O reaction rate: a change in this rate within the current experimental uncertainties may change the nucleosynthesis production factors by more than a factor of 2 [3]. The carbon to oxygen ratio, which is set by the ^{12}C(α,γ)^{16}O reaction also has extreme

consequences in the structure and evolution of late stellar burning stages and explosive scenarios. For example, the minimum main sequence stellar mass required to form a core collapse supernova depends on the core mass, which is determined by this reaction rate as well. In a similar way, hypernovae, collapsars, magnetars and their connection with gamma ray bursts depends on the core mass as determined by the $^{12}C(\alpha,\gamma)^{16}O$ at helium burning of the progenitors [4].

The $^{12}C(\alpha,\gamma)^{16}O$ reaction also has cosmological implications. Thermonuclear supernovae have been used as "standard candles" to determine the distance to galaxies and the rate of expansion (Hubble constant) of the universe [5]. It is thought that calibrated light curves of SNIa have consistent shapes, luminosity, and spectra that could be modeled if the C/O ratio in the progenitor is known. One of the leading Type Ia supernovae models is the combustion of a white dwarf in a degenerate state. Either from accretion from an evolved companion star or by merging with another white dwarf, a thermonuclear supernova will yield most of its mass as ^{56}Ni, the nucleus at the top for the α chain. The luminosity of the event is determined by the amount of ^{56}Ni produced, which decays sequentially to ^{56}Co and then to ^{56}Fe. It is the ^{56}Ni to ^{56}Co β-decay that determines the shape of the light curve observed after the explosion. The shape of the curve correlates very strongly with the luminosity of the event, so in spite of having "non standard" luminosities, these cosmological "standard" candles can be corrected to some degree to represent consistent distance indicators. Nevertheless, within the experimental error bars of the rate for the $^{12}C(\alpha,\gamma)^{16}O$ reaction, the amount of ^{56}Ni produced in these events can vary up to 10%, affecting the cosmological distance determination as a result[6].

Stellar evolution models in which nuclear reaction networks are implemented in detail still do not yield consistent results. The cross section for the $^{12}C(\alpha,\ \gamma)^{16}O$ reaction is probably one of the most important nuclear physics input parameter uncertainty that needs to resolved. Extensive work regarding this reaction has been done both by theorists and experimentalists. However, the tiny cross sections involved have proven to be a major obstacle in constraining the size of its error bar. Much work is still needed to improve the situation.

The level scheme of ^{16}O is shown in figure 1. The α-particle threshold (7.162 MeV) is very close and above the 6.197 and 7.117 MeV doublet in ^{16}O so that the helium burning Gamow window (shown in red, at about 300 keV above the threshold) is dominated by the tails of these subthreshold resonances. The Coulomb barrier at such low energies reduces the reaction cross section to values as low as 1×10^{-17} barn, making it impossible to measure with current technologies. Therefore, the value of the cross section at stellar temperatures needs to be constrained both by theory and measured values of the cross section at higher energies. The current situation for the E1 component of $^{12}C(\alpha,\gamma)^{16}O$ is shown in figure 2. Here,

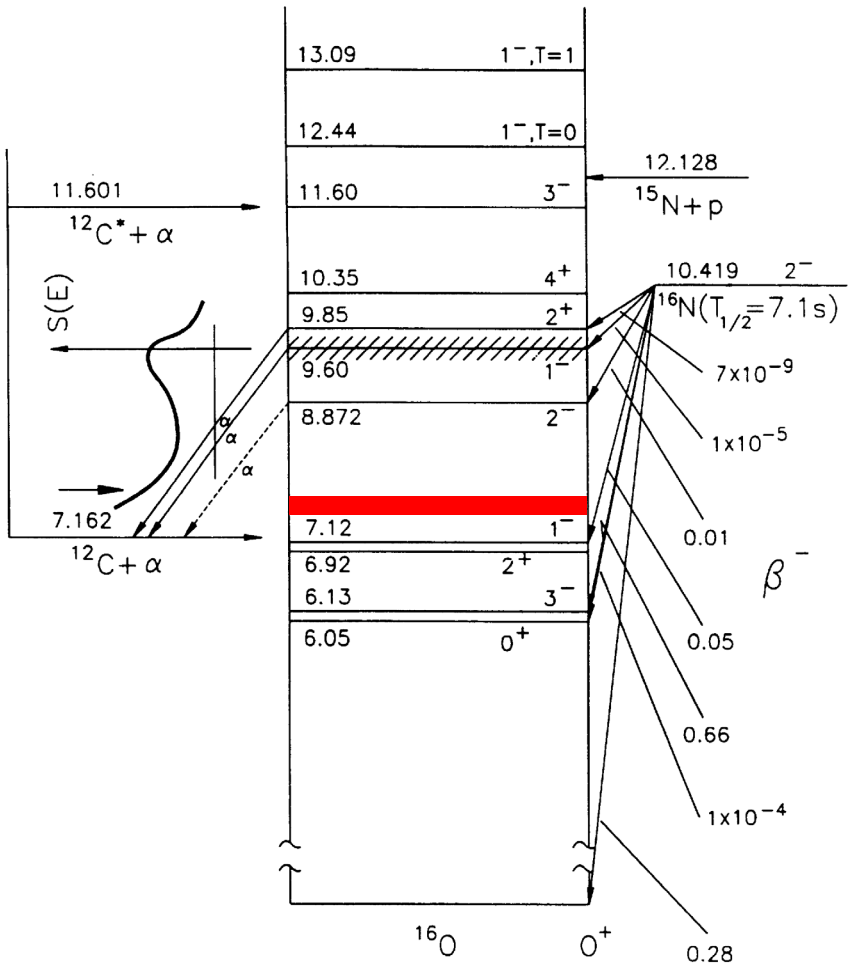

Fig. 1. Level scheme of ^{16}O. From [7]. The red region corresponds to the energy relevant for helium burning temperatures.

the S-factor S(E)=Eσ(E)exp($2\pi\eta$), with η the Sommerfeld parameter, has been plotted. The strong energy dependence of the cross section due to the Coulomb repulsion between nuclei pairs is removed by plotting S(E) instead of σ(E). However, one must remember that it is the cross section σ(E) what ultimately enters into the computation of the reaction rate $\langle\sigma v\rangle$.

Direct measurements of ^{12}C(α,γ)^{16}O extend down to 900 keV in the center of mass. These include both forward and inverse kinematics experiments that have suffered not only from the low γ-ray yield but also from ^{13}C-contaminated carbon targets that produce neutrons

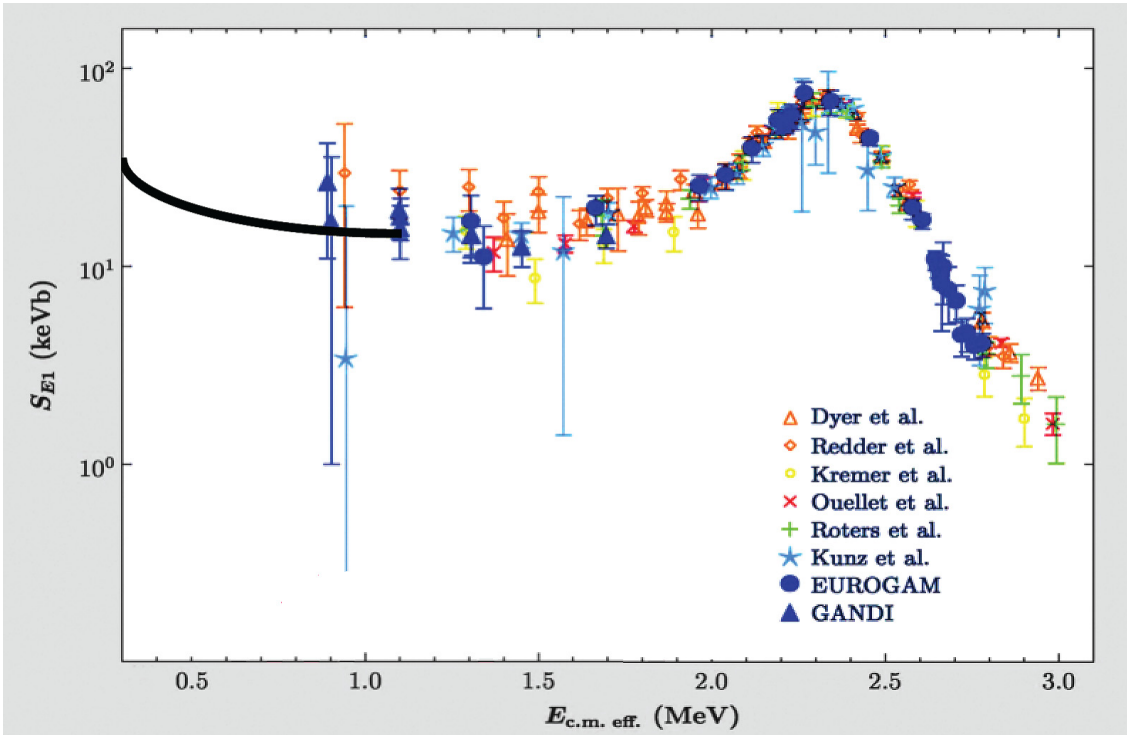

Fig. 2. The S-factor for the E1 component of the $^{12}C(\alpha, \gamma)^{16}O$ reaction. Data points correspond to some of the latest experimental direct measurement results. The solid line through the data represents one of many possible extrapolations into the astrophysically relevant energy region (~300 keV).

(e.g. $^{13}C(\alpha,n)^{16}O$), target thickness changes by carbon buildup, the low density of helium gas targets, beam induced and room γ-ray backgrounds.

Extrapolations of the S-factor down to 300 keV require a careful treatment of interferences between direct capture components and individual resonance contributions. If differential cross sections have been measured instead of the cross section integral, interferences between E1 and E2 components need to be considered as well. The standard theories for accounting for these effects are the R- and K-matrix formalisms of nuclear reactions. In some cases, the theoretical development of these theories has been driven by the analysis of the $^{12}C(\alpha,\gamma)^{16}O$ reaction itself [8–11]. For example, it has been found that the inclusion of elastic scattering data into the analysis can significantly constrain the extrapolation of the S-factor into the unmeasured energy region [12–14].

Indirect measurements involving α-particle transfer reactions (for example, $^{12}C(^{6}Li,d)^{16}O$ and $^{12}C(^{7}Li,t)^{16}O$) have also proven to be helpful in constraining the α-particle widths of

the subthreshold states and the direct capture components [15]. β-delayed α-particle decay of ^{16}N (J^{π}=2^{-} in the ground state) has also provided tight constraints for the E1 component contribution [16,7,17].

Performing a direct measurement at astrophysically relevant energies is beyond our current technical capabilities and measurements using standard techniques (e.g. γ-ray detection with Ge detectors) have reached their limits. However, it has been proven that in the context of the R-matrix theory of nuclear reactions, better experimental data at the lowest energy possible would improve the quality of the extrapolation of the cross section significantly.

2 Method

The new method is based on two principles: the reciprocity theorem for nuclear reactions, which relates the cross sections of forward and time-inverse nuclear processes, and the ability of a superheated liquid to induce nucleation when exposed to radiation [18]. Reciprocity allows one to deduce the cross section σ_A for particle capture (X,γ) processes to the ground state by measuring the cross section σ_B for photodisintegration (γ,X) reactions, i.e.

$$\omega_A \frac{\sigma_A(X,\gamma)}{\lambda\!\!\!^{-2}_{\alpha}} = \omega_B \frac{\sigma_B(\gamma,X)}{\lambda\!\!\!^{-2}_{\beta}}, \tag{1}$$

where X is the captured particle, $\lambda\!\!\!^{-}_{\alpha}$ and $\lambda\!\!\!^{-}_{\beta}$ are the channel wavelengths for capture and photodisintegration, and ω_A and ω_B are their respective spin factors. In the energy regimes discussed here, the transformation factor can provide a gain of over two orders of magnitude in cross section.

Capture reactions, such as (α,γ), (p,γ), and (n,γ), are responsible for many nucleosynthetic processes occuring in stellar environments. This is the case for the s and the α processes. Cases for which the reaction product is long lived can be studied experimentally by photodisintegration of the residual if a suitable target can be produced. When nuclei are photodisintegrated, the residual particles acquire an energy that adds up to the Q value of the reaction. If the energy of the γ ray is small compared to the mass of the target (this is the case for energies of relevance in astrophysics) the recoil energy is very small and for practical purposes it can be disregarded.

When a particle moves in a liquid, it deposits energy along its track until it is stopped. If enough energy is deposited in a short distance (linear density of energy deposition, or

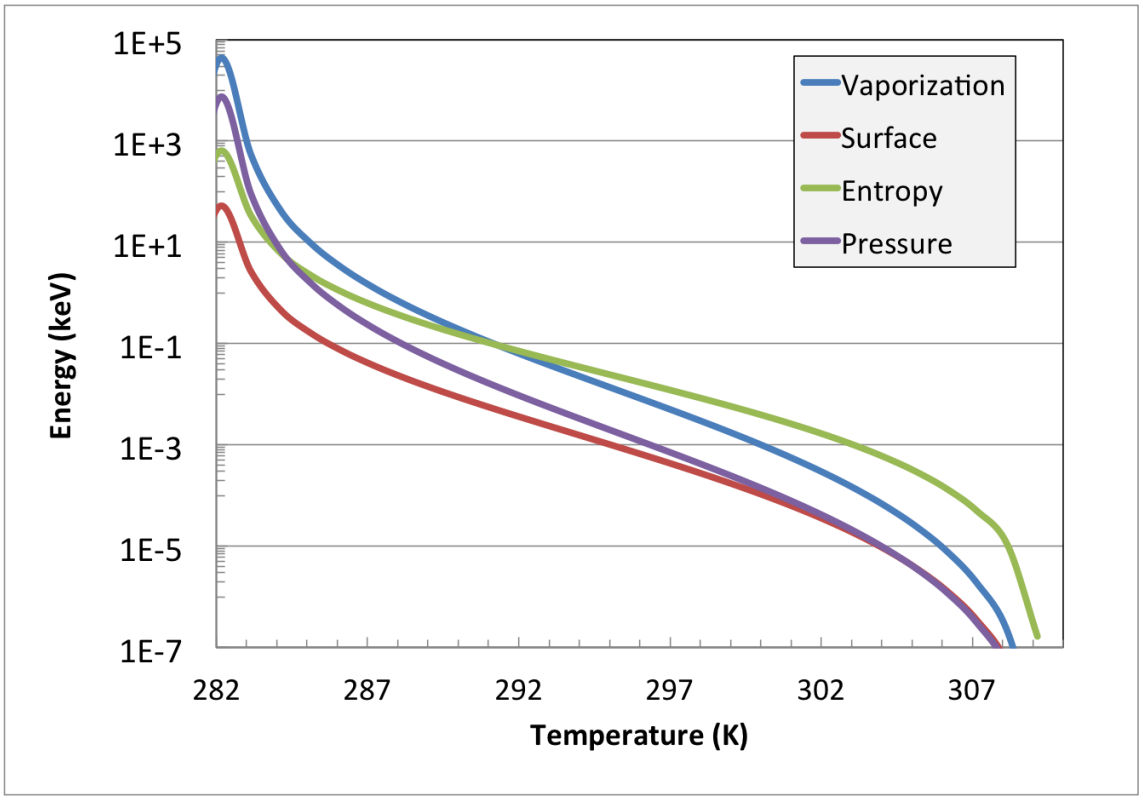

Fig. 3. Energy required to induce nucleation in N_2O with the individual contribution of the various terms in equation 4. The pressure is constant at 4.03 MPa. The curves span from the saturation point to the critical point.

stopping power dE/dx), the liquid will be vaporized and a bubble will be formed. This is the "temperature spike" model of bubble formation [19]. Not all bubbles formed by this mechanism will eventually grow to become visible. In order to form a macroscopic bubble (a bubble visible to the unaided eye) enough energy E_c must be made available by the particle to form a bubble of critical radius

$$R_c = 2s/(P_v - P), \tag{2}$$

where P_v and P are the pressures of vapor and the liquid, respectively, and s is the surface tension of the liquid. The total energy and stopping power threshold conditions can be expressed as

$$\frac{dE}{dx} \geq \left(\frac{dE}{dx}\right)_c = \frac{E_c}{aR_c}, \tag{3}$$

and

$$E \geq E_c = \frac{4}{3}\pi R_c^3(\rho_v h + P) + 4\pi R_c^2\left(s - T\frac{\partial s}{\partial T}\right), \tag{4}$$

where ρ_v is the density of vapor, h is the enthalpy of vaporization, and T is the temperature of the liquid. The first term to the right is a volume term that accounts for the energy necessary to vaporize the liquid inside a bubble of radius R_c and the energy necessary to expand the bubble against the liquid pressure. The second term describes the energy necessary to form the bubble surface. It includes an entropy contribution $T\partial s/\partial T$. The several contributions are shown in figure 3 for the liquid N_2O at a pressure of 4.03 MPa, which is typical of the operation of a bubble chamber using this liquid. Once the bubble has reached its critical size, as the liquid is superheated, the pressure of the gas inside the bubble will be larger than the pressure of the liquid around it and the bubble will continue growing. Vaporization of the whole volume of the liquid will occur unless the superheat is removed from the system. In practice this is done by a prompt pressurization of the liquid.

The process of preparation of this metastable state in liquids is shown in figure 4 for water. First, the liquid is pressurized at ambient temperature (1 to 2), then the pressure is kept constant while the temperature is increased to above the boiling point (2 to 3), and finally, the pressure is slowly released while keeping the temperature constant (3 to 4). At this point (4), water is still liquid but now superheated. It takes only a small disturbance to induce vaporization at this state. When this happens the bubble growth process needs to be controlled by increasing the liquid pressure (4 to 3). It usually takes about one second for the liquid to return to a stable state (this depends mostly on the volume of the liquid being superheated and the maximum size reached by the bubble). Superheat is then returned into the system by releasing the pressure again (3 to 4), and the cycle is repeated for each bubble event in the detector.

The two threshold conditions from equations 3 and 4 are functions of the operating pressure and temperature of the liquid. Therefore, it is possible to tune the sensitivity of the detector to reject some minimum ionizing particles, while making it sensitive to heavy ions. Also, the detector is insensitive to the γ-ray beam at least at a level of one part in 1×10^9 [20]. However, there is one free parameter a in the theory. It relates the critical size bubble with the length L over which the particle transfers energy to the liquid by $L=aR_c$ [21]. This free

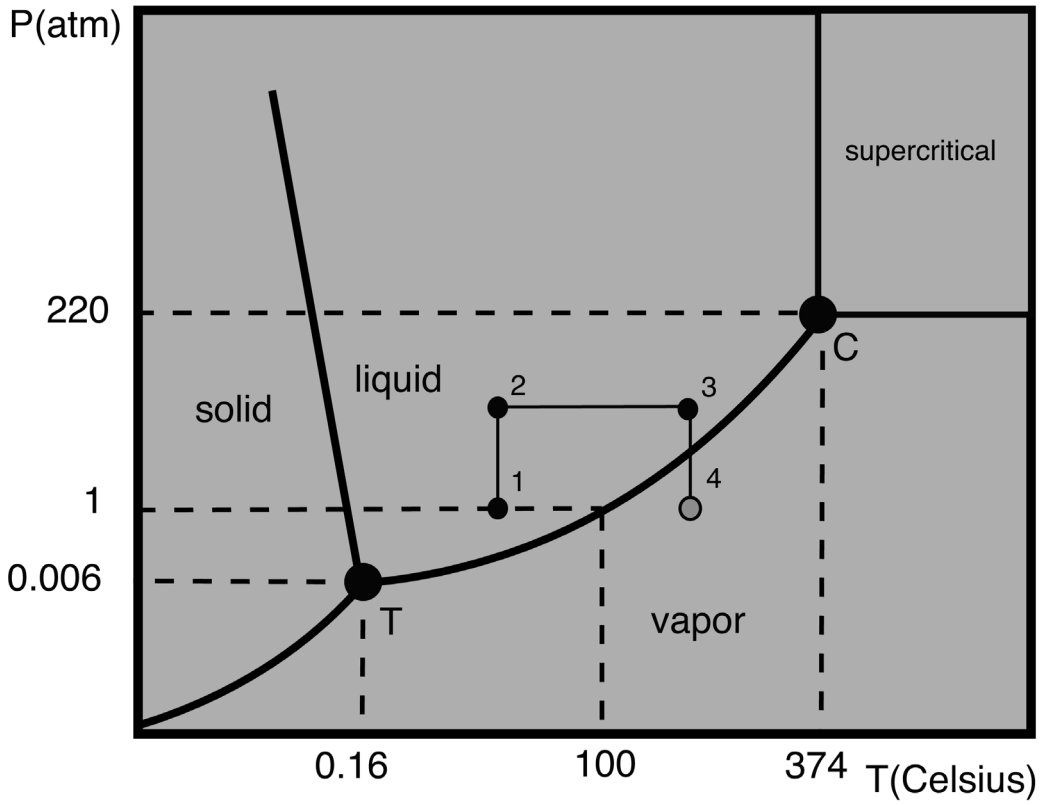

Fig. 4. Phase diagram for water. The path illustrates the method for superheating a liquid and the operation (pressure and temperature cycle) of the bubble chamber.

parameter is a property of the liquid that needs to be determined experimentally.

Figure 5 shows an example of stopping power curves for some ions in the liquid N_2O, as calculated with SRIM [22]. The horizontal solid black line and dashed black line are the stopping power threshold calculated with two different models [23,21]. The energy threshold is represented by the solid vertical line at 4.2 keV. Particles above the horizontal threshold $(dE/dx)_c$ and to the right of the vertical E_c threshold will induce nucleation. The thresholds can be adjusted by changing the pressure and temperature conditions of the liquid, so that some ion species can be discriminated while others detected. For example, carbon ions produced from the photodisintegration of ^{14}N and ^{16}O at E_γ=8.5 MeV are shown by the triangle and diamond symbols in the plot. The stopping power thresholds are such that events from ^{14}N are rejected while those from ^{16}O nucleate. Moreover, the γ-ray

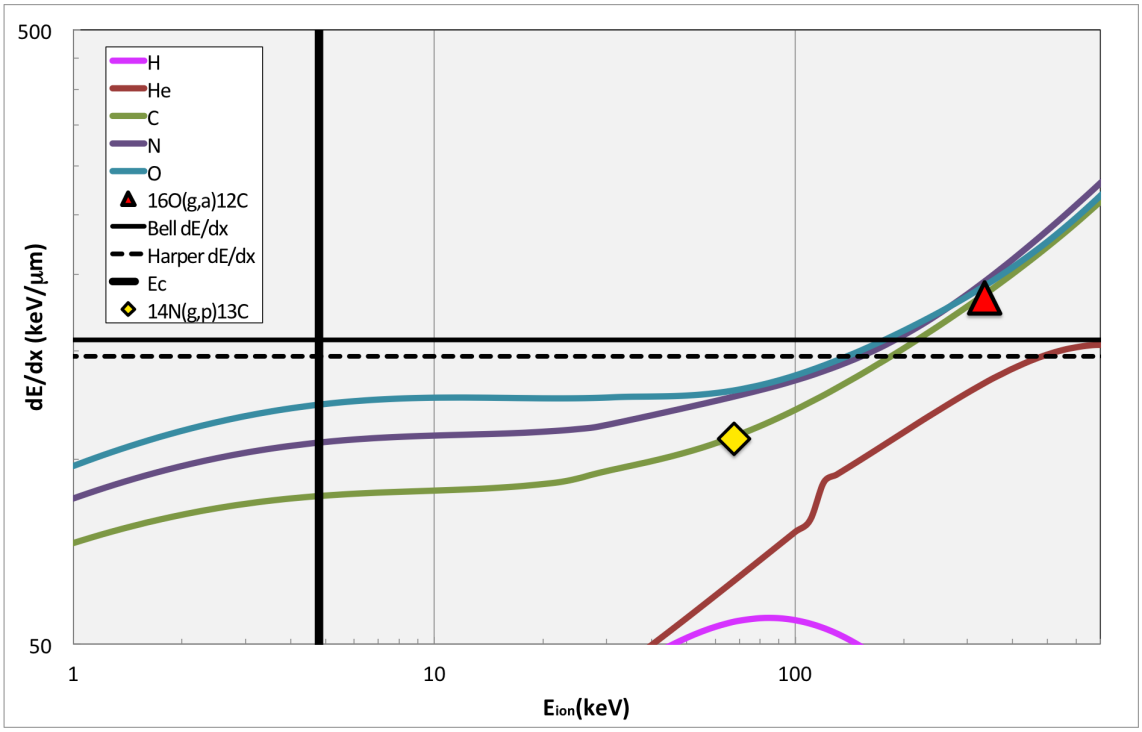

Fig. 5. Nucleation thresholds for the liquid N_2O at P = 4.03 MPa and T = 287 K. See text for details.

beam passes through the detector without triggering bubble formation at all.

The energy loss for electrons, neutrons, and γ-rays is very small and does not appear in the plot. However, these particles may transfer their momentum to other ions by scattering interactions. While being insensitive to neutrons, bubble chambers can be triggered by them when they elastically scatter from the nuclei in the superheated liquid. Neutrons are useful in the calibration of the detection thresholds, however, they are also important background sources that need to be well understood in this kind of experiments. The dE/dx threshold condition for N_2O is very sharp, with a transition slope from no nucleation to full nucleation of only a few keV/μm, reaching a full nucleation efficiency of 100% [24]. This has been studied elsewhere [25] and it is consistent with our observations.

We determined the free parameter in the theory for N_2O by exposing the bubble chamber to a monoeneretic γ-ray beam produced by the HIγS facility. By keeping the temperature of the liquid at a fixed value, the operating pressure was lowered from the saturation curve to a pressure at which the bubble chamber started triggering nucleation. This determined the (P,T) conditions at threshold. The free parameter in the theory is then uniquely determined by the (P,T) conditions and the energy of the ions triggering nucleation. We determined

the parameter to be a=3.6±0.5. This measurement is necessary to select the operating conditions of the liquid that would make it sensitive to some reactions, while rejecting some other sources of background.

One disadvantage of the proposed technique is its inability to measure contributions to the reaction cross section coming from transitions different from the ground state. Our method only examines the (α,γ_0) cross section. For the special case of the $^{12}C(\alpha,\gamma)^{16}O$ reaction, the so-called cascade transitions have been proposed to contribute a 12% or 19% to the reaction cross section at astrophysical energies, depending on the sign of the reduced width amplitude of the direct component used in the R-matrix analysis, either negative, or positive, respectively [26]. However, a more recent study claims a contribution of all cascades to the ground state to be as small as 3% [27].

3 Detector

The selection of the liquid to be used in the bubble chamber depends on several factors. Foremost, the molecular content of target ions whose photodisintegration cross section needs to be determined has to be maximized. Other ions present in the molecule of the liquid may be sources of background. Ideally, pure targets are desirable. However, trace contaminants always exist, or the operating (P,T) conditions of the pure target in liquid form may be too extreme to work in a practical device. This is why usually the liquid of choice consists of more than one ion species. In principle, all liquids should nucleate in bubble chambers [28]. It is a matter of convenience to select materials that are liquid at normal pressure and temperature conditions.

Transparent liquids are also a convenient choice as optical imaging techniques can be applied to detect the bubble events and trigger the pressure system that stops bubble growth and vaporization of the whole liquid volume. This also requires the transparency of the vessel containing the superheated liquid, strongly constraining the material of choice seen by the beam before and after it reaches the sensitive liquid. Another promising technique for detecting bubble formation that does not have the transparency requirement is the detection of the sound produced by the fast and violent growth of the bubble in its early microscopic state. The disadvantage of this technique is that spatial resolution is well behind that of the optical method.

Also fundamental is the fact that the liquid to be superheated will need to be pressurized, as discussed in the previous section. This is usually done with a pressure transfer fluid

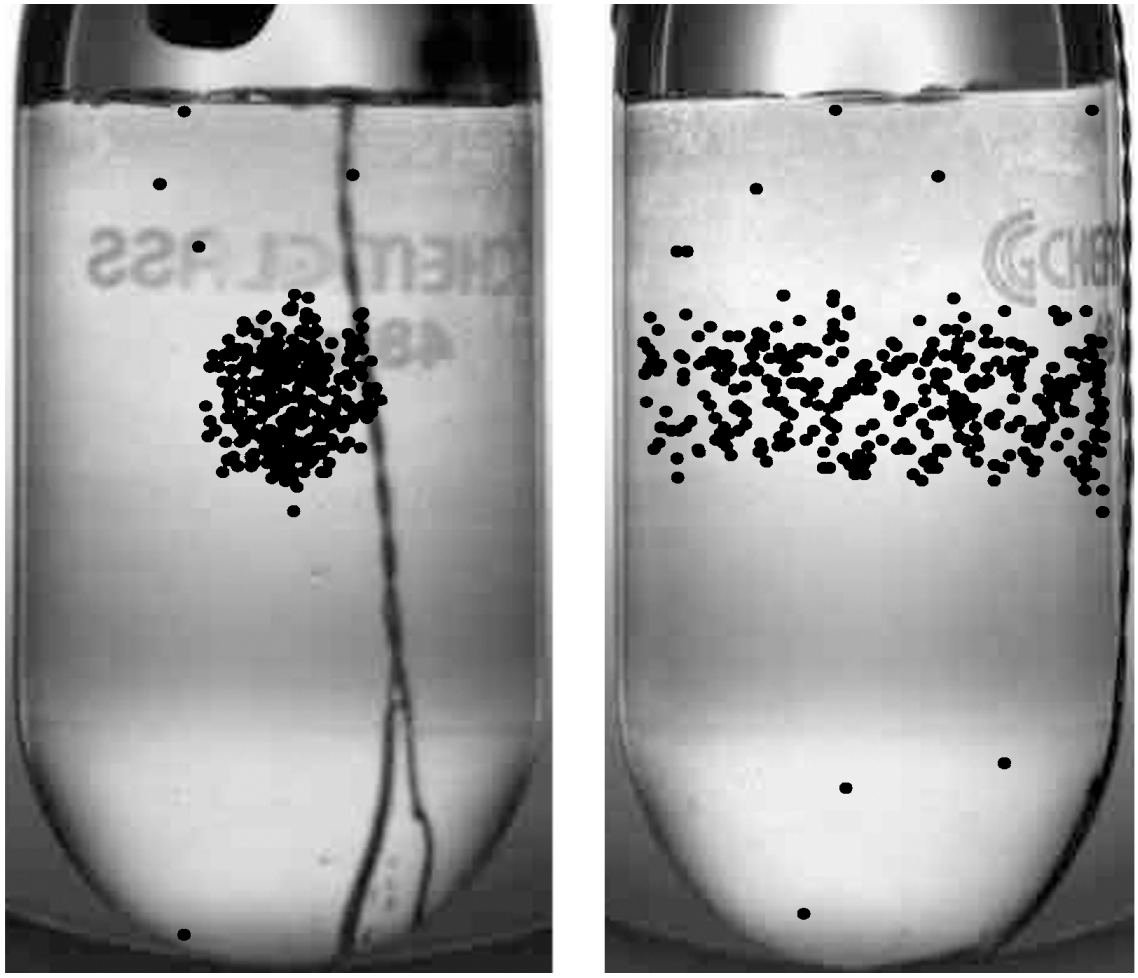

Fig. 6. Target vessel of the bubble chamber irradiated with a narrow band γ ray beam from HIγS. Black dots show the sites of bubble formation for a γ-ray beam at energies between 8.7 and 10.0 MeV integrated over a period of 12 hours. The beam intensity was 4×10^3 γ/s and the liquid was the refrigerant R134a. Events outside of the beam region correspond to background from neutrons produced by cosmic rays and /or the walls of the experimental hall. The beam region contains photodisintegration events mainly from ^{19}F(γ,α)^{15}N and an estimated 2% of cosmic ray induced background. The camera was placed at 45° relative to the beam direction.

that is put in contact with the sensitive liquid. For the case of a water bubble chamber a possible transfer fluid is oil that does not become superheated at pressure and temperature conditions for superheated water. The two liquids would need to have a minimal solubility into each other.

As opposed to conventional active gas targets frequently used in disintegration experiments,

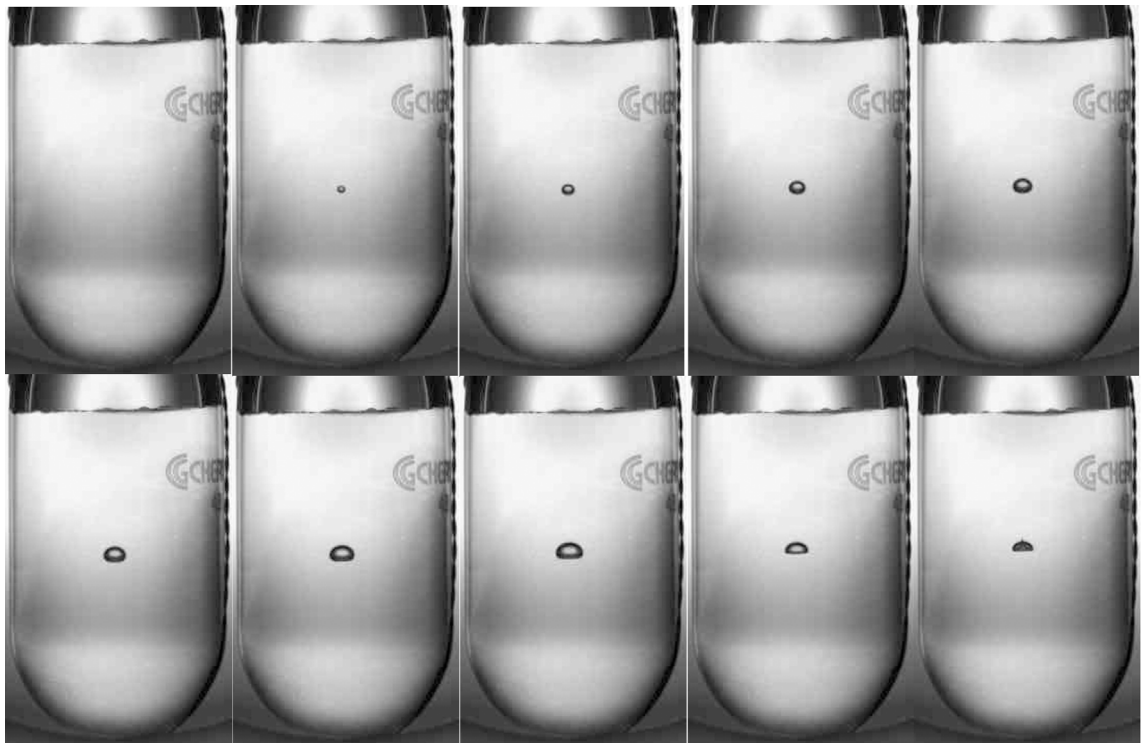

Fig. 7. Photograph sequence of an event registered by a 100 Hz video camera. The whole set spans 0.1 s, at equally spaced time intervals. The bubble was induced by ^{15}N from the ^{19}F(γ,α)^{15}N reaction. Bubble detection is triggered by comparing the first two pictures in the sequence. Later on, at about 60 ms, the system responds by quenching the bubble until it disappears, about another 100 ms later.

the liquids used in bubble chambers typically have densities a factor of 10^4 to 10^6 higher. This implies that the experimental yield obtained using a bubble chamber scales accordingly, considerably reducing the time the target needs to be exposed to the beam and making the bubble chamber a device worth considering when measuring very small cross sections.

A nucleus photodisintegrated at several MeV γ-ray beam energies (of the kind of relevance to the type of experiments proposed here) will produce recoil products of some hundreds of keV to a few MeV in energy. This is very small compared to the high energy of particles that have been studied classically with bubble chambers. In those cases, particles leave behind bubble tracks that can be used to identify the nature of the events. However, the kind of experiments of interest here produce single bubble events that reflect the microscopic short range of the sources of nucleation (see figure 7). In this early version of the bubble chamber, a C_4F_{10} liquid is contained in a cylindrical glass vessel with a length of 10.2 cm and an outer diameter of 3.8 cm. Pictures of the superheated liquid are taken at 10 ms intervals

by two CCD cameras mounted at 90° relative to each other. The images are then analyzed in real time by a computer and when a bubble is detected, the pressure in the glass vessel is increased within 40 ms of bubble formation from 54 kPa to 793 kPa. This leads to a quenching of the growing bubble thus preventing a boiling runaway of the liquid. The size of the bubbles is typically 1 to 2 mm in diameter after 40 ms. Their location is determined to a precision better than 1 mm. The spatial resolution is fundamental for the discrimination of some backgrounds, as discussed below.

4 Previous experiments

The concept for measuring cross sections for photon induced processes has been tested [29] by exposing the bubble chamber to γ-rays produced with the HIγS facility at Duke University [30]. The narrow bandwidth photon beam was generated by intracavity Compton backscattering of free-electron-laser light from high-energy electron beam bunches. This photon beam was collimated with a series of three, 10 cm long, copper cylinders with a 1 cm circular hole and aligned at 0° with respect to the electron beam axis. The first collimator was located 52.8 m downstream from the collision point. We operated the storage ring in asymmetric two-bunch mode in order to reduce the beam energy spread.

The proof of principle of the technique was provided by comparing the count rate obtained in the detector while the γ-ray beam hit the superheated liquid against the count rate registered while no beam was produced by the accelerator. The spatial distribution of the events obtained from the cameras correlated very well with the 1 cm diameter size and position of the γ-ray beam (see figure 6).

The beam intensity was measured with a high-purity germanium detector placed downstream of the target. A thick aluminum absorber was placed between the bubble chamber and the γ-ray detector in order to limit the high photon flux incident on the detector crystal. The γ-ray spectrum was corrected with a Monte Carlo simulation of the response function of the detector and the attenuation in the absorber. The resulting spectrum then represents the γ-ray beam incident on the bubble chamber (see inset in figure 8). The beam intensity ranged from 2×10^3 γ/s to 3×10^6 γ/s, with a systematic error in its determination better than 5% [31]. The beam energy spread was kept below 2%.

The cross section obtained from the ^{19}F(γ,α)^{15}N reaction converted to the ^{15}N(α,γ)^{19}F scale using equation 1 is given by the points in figure 8. The thick solid line is the result of a calculation using the resonance parameters of the ^{19}F states in the E_x=5-6 MeV range obtained

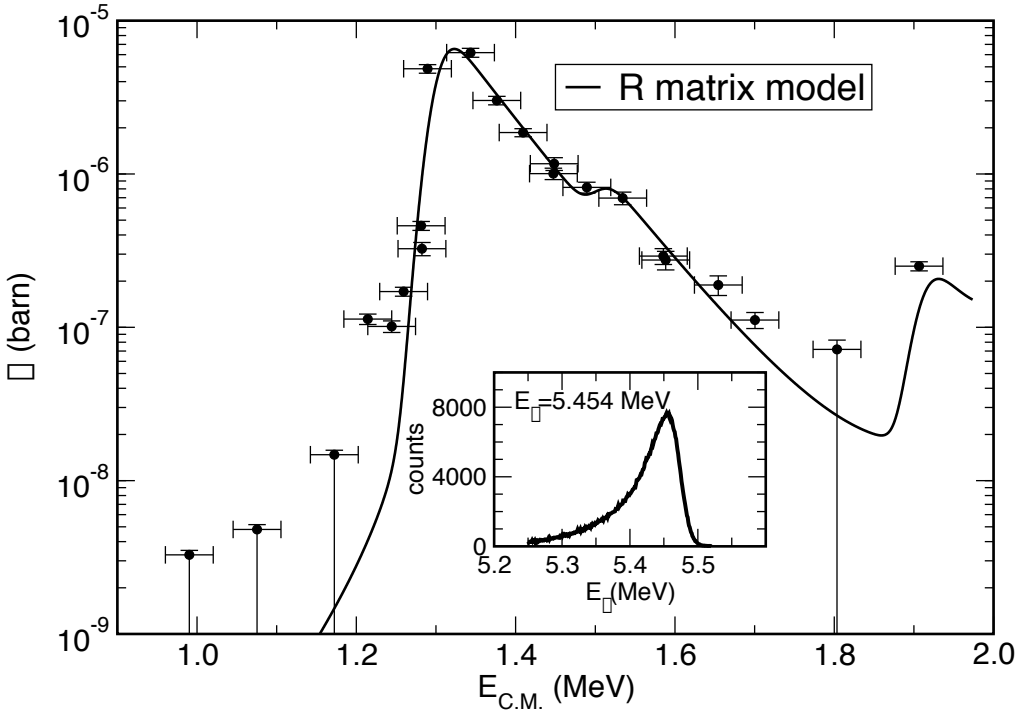

Fig. 8. Excitation function measured with a C_4F_{10} bubble chamber at E_γ=5.0-6.0 MeV ($E_{C.M.}$=1.0-1.9 MeV). The curve represents a model of the $^{15}N(\alpha,\gamma)^{19}F$ reaction convoluted with the γ-ray beam profile. The inset shows the profile of an example of HIγS γ-ray beam (centroid at E_γ = 5.454 MeV) impinging on the bubble chamber[29].

from the direct $^{15}N(\alpha,\gamma)^{19}F$ measurement of Ref. [32] and folding Breit-Wigner resonances with the energy profile of the γ-ray spectrum (inset in figure 8). There is an excellent agreement between the results of the direct (α,γ) measurement and the time-inverse (γ,α) experiments. The cross section measured covers more than three orders of magnitude, ranging from about 3 nb to about 10 μb, with the point at the lowest energy corresponding to 242 counts accumulated in 35 minutes. Also, the excellent agreement between this experiment and previous work confirms the expectation that the bubble chamber is 100% efficient

The systematic error in the determination of the cross section was largely dominated by the dead time uncertainty of the bubble chamber. A dead time of two seconds was determined by sampling the pressure in the bubble chamber at a rate of 1 kHz after each event trigger.

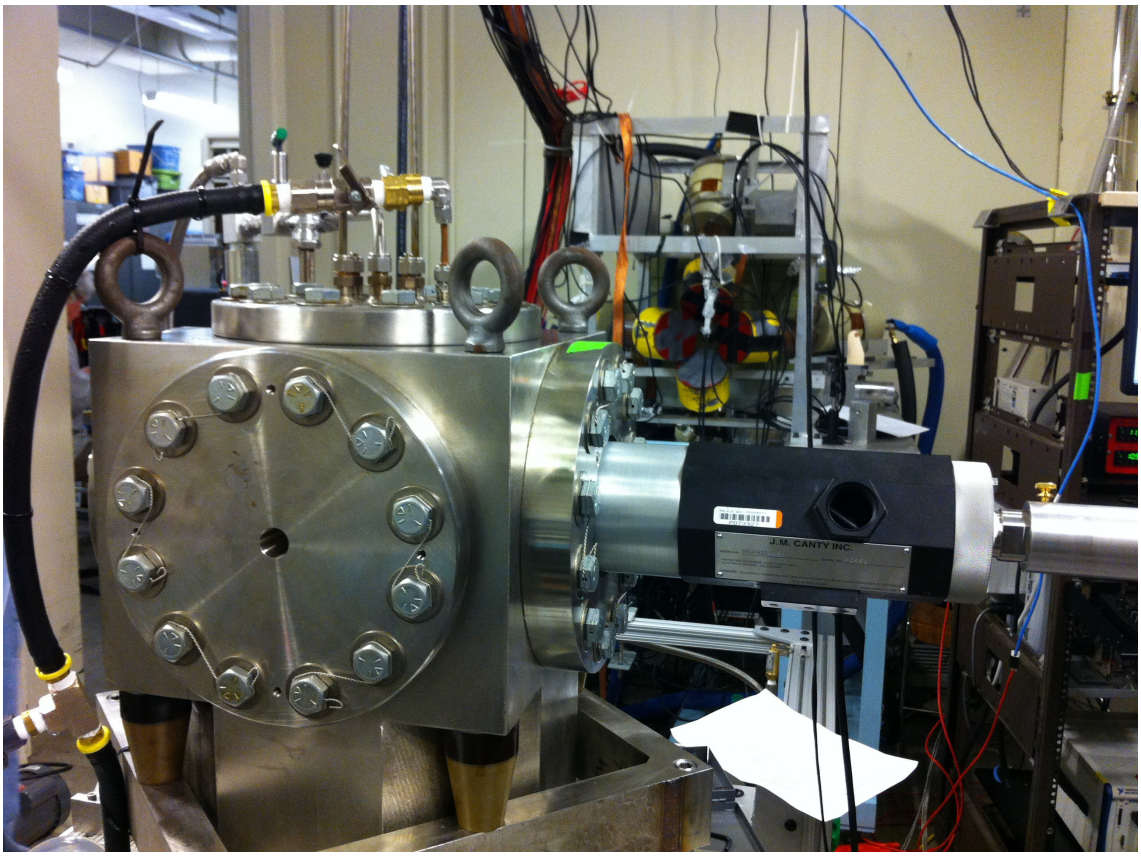

Fig. 9. Bubble chamber for the oxygen containing liquids CO_2 and N_2O used in April 2013.

The count rate at the lowest cross section measured was typically 0.11 counts/s at an incident flux of 3×10^6 γ/s, demonstrating the high luminosity that has been achieved with the bubble chamber. The count rate tolerated by the bubble chamber ranges from 0.5 events per second down to 1 count per minute, or longer. This is limited by the level of background obtained in the experiment.

With the successful completion of the $^{19}F(\gamma,\alpha)^{15}N$ experiment we have turned out attention to the $^{16}O(\gamma,\alpha)^{12}C$ system. The first question concerns the choice of an oxygen containing liquid. Below we have summarized the various liquids considered so far. The critical parameters in choosing the best liquid include the purity (i.e. presence of other nuclei such as C, N, H,..), critical pressures, temperatures, flammability, etc. In addition one has to consider that in the final experiment highly enriched ^{16}O has to be used, since reactions on $^{17,18}O$ have large (γ,α) cross sections. The liquids that were considered and their critical points include:

- Liquid oxygen (LOX) (T_C=-118.6 °C)
- H_2O (T_C=373 °C)
- CO_2 (T_C=31 °C)
- N_2O (T_C=36.4 °C)
- CH_3OH (T_C=240 °C)

Toxicity and safety issues eliminated other possible choices such as NO, NO_2, H_2O_2.

LOX: Considering contamination from other elements liquid oxygen would be the best choice, but it requires building a cryogenic continuously working bubble chamber. Cryogenic hydrogen bubble chambers have been used in the past, but to our knowledge they only operated in pulsed mode, i.e. they were not continuously active. Considerable R&D would be needed to construct a continuously operating bubble chamber with liquid oxygen.

H_2O: Water requires relatively high pressures and temperatures (T 200-250C), but it has the advantage that only hydrogen is present as a contaminating element. We have purchased 5 liters of ^{16}O water with upper limits (measured with standard mass spectrometers) for D/H and $^{17,18}O/^{16}O$ in the 10^{-6} range. More precise values will be obtained using Accelerator Mass Spectrometry techniques.

CO_2: Carbon dioxide becomes superheated at relatively low temperatures, but the presence of ^{12}C with a relatively low α-particle breakup energy of 7.37 MeV requires a separation of the $^{16}O(\gamma,\alpha)^{12}C$ events from $^{12}C(\gamma,3\alpha)$. While the use of $^{13}CO_2$ eliminates interference from the $^{12}C(\gamma,3\alpha)$ breakup the low (γ,n)-threshold (4.946 MeV) leads to neutron production that can generate additional backgrounds. As all other possible liquids it also requires high enrichment in ^{16}O.

N_2O: Nitrous oxide is similar to CO_2 in its thermodynamic properties. The threshold for $^{14}N(\gamma,p)^{13}C$ is slightly higher than the triple-alpha threshold in ^{12}C, but the cross sections above the $^{14}N(\gamma,p)^{13}C$ (threshold 7.55 MeV) are quite large. A reduction of this background should be possible by choosing the right pressure and temperature conditions for the superheated liquid.

Methanol: Flammability issues make these liquid less ideal for a bubble chamber.

From these five liquids we have studied H_2O, CO_2 and N_2O. Since all of these liquids have critical pressures above 40 atmospheres, a high pressure vessel was built. It consists of a thick-walled stainless steel pressure vessel filled with mineral oil. Inside the pressure tank is a glass vessel containing the superheated liquid and a so-called buffer fluid, which minimizes the amount of the superheated oxygen-containing fluid, which, since it requires enriched isotopes, can be quite expensive. The pressure is transferred from the oil to the superheated liquid via a stainless steel bellows. Bubbles occurring in the superheated liquid are observed with a fast CCD camera (frame rate of 100 Hz) mounted behind a 5 cm thick high-pressure glass window.

While H_2O at T=200-250 °C worked well as a liquid for a continuously operating bubble chamber we observed after a few hours of operation an etching of the interior glass vessel (most likely caused by HF formed between the fluorine containing buffer fluid and the superheated water) which blocked the view for the CCD camera and furthermore lead to bubble formation at the glass surface.

We therefore decided to try the other two liquids, CO_2 and N_2O, which required a change of the system from heating to cooling (the critical temperatures are 31°C and 36.4°C, respectively). No continuously operating bubble chambers with these liquids have ever been built. The main difference to bubble chambers operating with refrigerants or water is in the size of the bubbles, which are considerably smaller than the ones observed for the other liquids. This change in bubble size can be understood from the viscosity, thermal conductivity and surface tension of the liquids involved.

In our first engineering run at HIγS at the end of April 2013 we tried both liquids, CO_2 and N_2O. It was found that CO_2, while working well in a continuously operating bubble chamber, experiences another chemical complication originating from the formation of hydrates at low temperatures that changed the transparency of the superheated liquid. A buffer fluid different from water might avoid this complication. Since testing different fluids is a time consuming process we changed the liquid for the test run to superheated N_2O during the last two days of the experiment.

Both liquids share very similar thermodynamic properties, so from the engineering perspective they can operate in the same bubble chamber device (see figure 9). We operated these liquids at temperatures ranging from 10 to 15 °C, so the energy required to induce nucleation is relatively small due to the proximity of the critical point (see figure 3). Therefore, superheats of 3 to 4 °C are sufficient to detect photodisintegration events in the bubble chamber. The experiment is undergoing analysis (see figure 10).

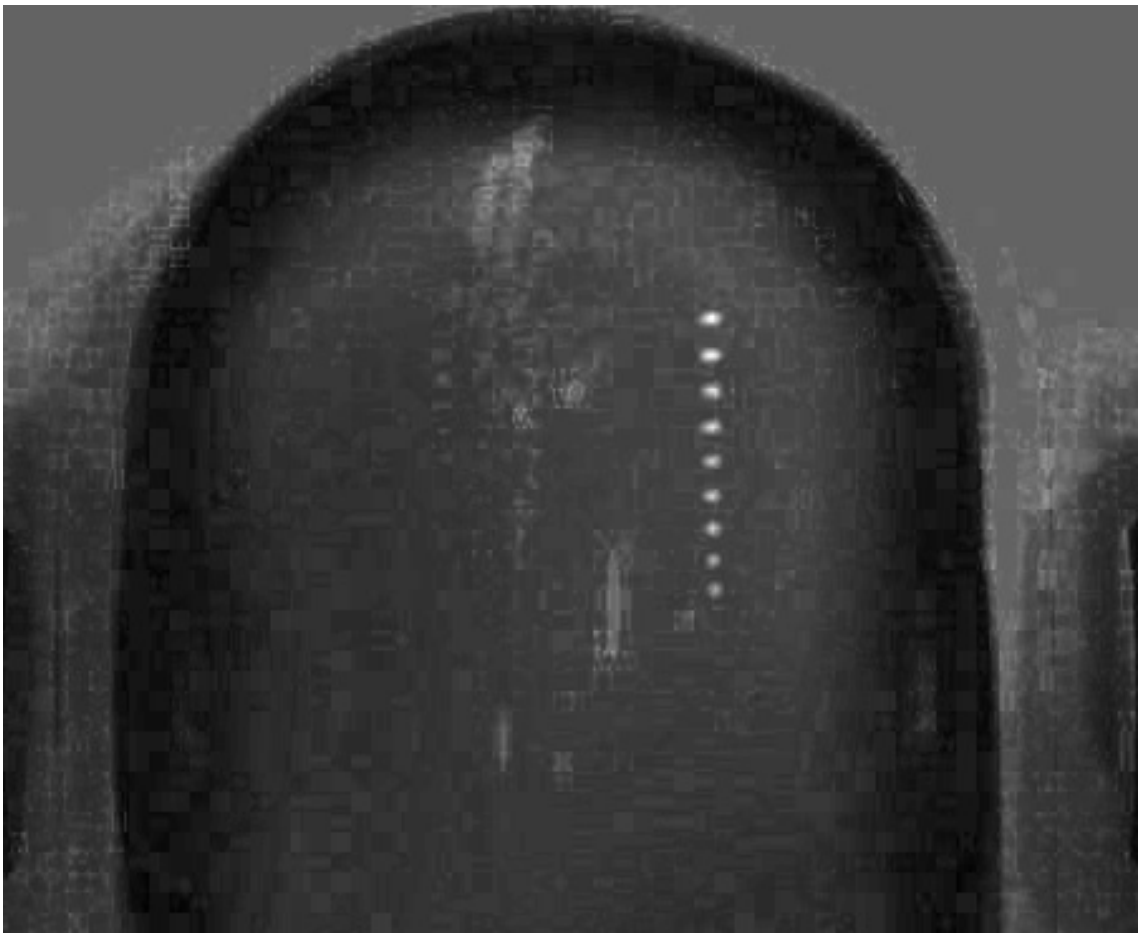

Fig. 10. Composite of nine sequential photographs taken at 10 ms intervals for the first $^{16}O(\gamma,\alpha)^{12}C$ event in the N_2O bubble chamber. The temperature was 11 °C at 3.79 MPa and the γ-ray beam energy was 9.66 MeV.

5 Backgrounds

For the type of experiments discussed here, it is useful to define two different kinds of background sources that can contribute to the bubble count rate in the detector. The first contribution produces events that are spread evenly over the whole volume of the sensitive liquid. The second produces events that appear in the same spatial region as the γ-ray beam inside the superheated liquid. The first type can be determined in a straightforward manner by two independent methods: first, the count rate of events appearing outside of the beam region is compared to that of events in the path of the beam, while the γ-ray beam is irradiating the target. This is one of the reasons for which a good spatial resolution

of the bubble chamber is required. In the experiment, this background contribution was determined to be about 8% of the count rate registered outside of the beam region. This value is in good agreement with the background observed in a second method, where the bubble chamber was moved to the side of the beam so that the liquid was not in the path of the γ rays. Sources of this background are fast neutrons produced by cosmic rays and by the photodisintegration of beamline and accelerator materials that are scattered into the bubble chamber. This background contribution can be reduced by passively shielding the bubble chamber detector with a neutron absorbing material.

The other background source cannot be easily corrected for by using the information from the fiducial volume. These background events are produced in the same spatial region as those from the photodisintegration reaction of interest. The main contributors to the count rate in this case are other reactions induced by neutrons produced upstream in the beam line and collimated in the same region as the γ-ray beam. This set of background sources can be suppressed by a) choosing the threshold conditions in the bubble chamber such that their interactions do not trigger bubble formation, b) by a subtraction of yields in which contaminant reactions are carefully accounted for, c) by placing a neutron absorber upstream in the beam line, and d) by identifying the neutrons from the sound they produce when inducing nucleation in the superheated liquid [33]. This background source was also studied in the HIγS experiment.

We expect the neutron backgrounds to be minimal in the JLab experiment because the maximum electron beam energy is only 8.5 MeV and we have chosen materials such as nitrogen, Cu, and Al that have very high photoneutron thresholds. The main background found at the HIγS experiment arose from high energy bremsstrahlung from residual gas in the electron ring where the electron beam (400-500 MeV) at typically 40 mA circulating in the ring impinges on the residual gas. It is mainly for this reason that we have turned to exploring the use of low energy bremsstrahlung at JLab.

Photodisintegration events from nuclei in the superheated liquid are also possible sources of background. Some background sources for N_2O that has been depleted of ^{17}O and ^{18}O by a factor of 1000, are shown in figure 11. Some reactions such as $^{14}N(\gamma,p)^{13}C$, $^{29}Si(\gamma,n)^{28}Si$ (from silicon in the glass containing the liquid), and $^{17}O(\gamma,n)^{16}O$ have Q-values sufficiently high as to produce recoils that are slow and, thus, can be suppressed by setting the right (P,T) conditions of the bubble chamber. On the other hand, the heavy ions from reactions on the glass are stopped before reaching the superheated liquid, so they do not pose a background problem.

Electromagnetic debris such as degraded electrons, γ-rays, and positrons, may escape the

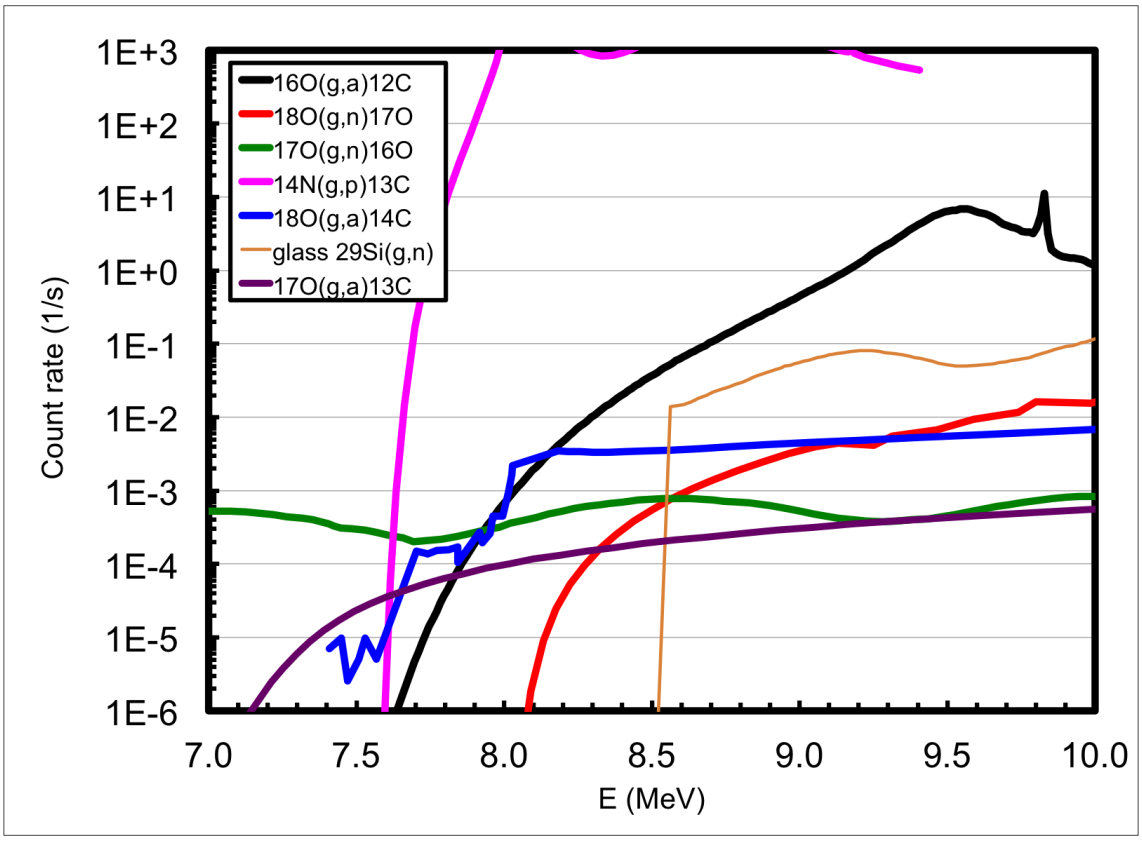

Fig. 11. Background contributions from photodisintegration of nuclei in the superheated liquid (N_2O that has been depleted of ^{17}O and ^{18}O by a factor of 1000). Curves assume a 10% detection efficiency for the photoneutron reactions on the glass container, and a 100% efficiency for other reactions. By choosing the bubble chamber thresholds discussed in section 2, background sources such as $^{14}N(\gamma,p)^{13}C$, $^{29}Si(\gamma,n)^{28}Si$, and $^{17}O(\gamma,n)^{16}O$ can be eliminated.

collimator and electron beam stop devices and irradiate the detector. However, these minimum ionizing particles do not induce nucleation on the bubble chamber as the operating conditions will be such that only heavy ions (see figure 5) will be inside the detection window. Therefore, these events are suppressed effectively by the choice of the detector superheat.

6 Proposed experiment

The bubble chamber will be installed in the 5 MeV region of the Jefferson Lab injector at the end of a beamline spigot used by the PEPPo Experiment. The PEPPo experiment is completed and is now being removed from the injector.

The nominal beam properties in the 3-8.5 MeV region are listed in Fig. 13. The absolulte beam energy is measured using the 5 MeV dipole and is known to about 1%. This dipole was mapped and the beam orbit through the magnet is measured using a set of beam position monitors on the main accelerator beamline and on the PEPPo spigot beamline. We are exploring ways to improve the determination of the absolute beam energy. The beam current is measured using a beam monitor located before the 5 MeV dipole. This monitor is used by the accelerator and the experimental halls and measures the beam current within 3%.

Table 1
Systematic error contributions.

Source	Systematic Error (%)
Absolute beam energy	11-28
Beam current	3
Photon flux	5
Radiator thickness	3
Target thickness	3
Bubble chamber efficiency	5

Table 2
Projected cross section systematic error due to a 0.2% energy error.

Energy (MeV)	Cross Section Error (%)
7.9	28
8.0	23
8.1	19
8.2	15
8.3	13
8.4	12
8.5	11

Table 3
Integrated beam current requirements per data point.

Energy (MeV)	Beam current (μA)	Beam time (h)
7.9	100	100
8.0	100	20
8.1	80	10
8.2	20	10
8.3	10	10
8.4	4	10
8.5	2	10

Table 4
Integrated yield per data point.

Energy (MeV)	Yield	Error
7.9	541	23
8.0	558	24
8.1	864	29
8.2	628	25
8.3	831	29
8.4	741	27
8.5	756	27

Table 5
Unfolded cross section per data point.

Energy (MeV)	Cross Section (nb)	Statistical Error (nb)
7.85	0.047	0.002
7.95	0.176	0.010
8.05	0.613	0.029
8.15	1.48	0.10
8.25	3.71	0.21
8.35	6.80	0.51
8.45	12.5	0.9

A schematic drawing of the experiment is shown in figure 12. The Bremsstrahlung beam will be generated using a 0.02 mm Cu radiator. A sweeper magnet after the radiator will bend the electron beam to a shielded local beam dump. The photon beam will exit the beamline vacuum through a 10 mil Cu vacuum window. We will use a Cu collimator to remove the large angle photons. After the bubble chamber, the photon beam will be dumped in an Al piece.

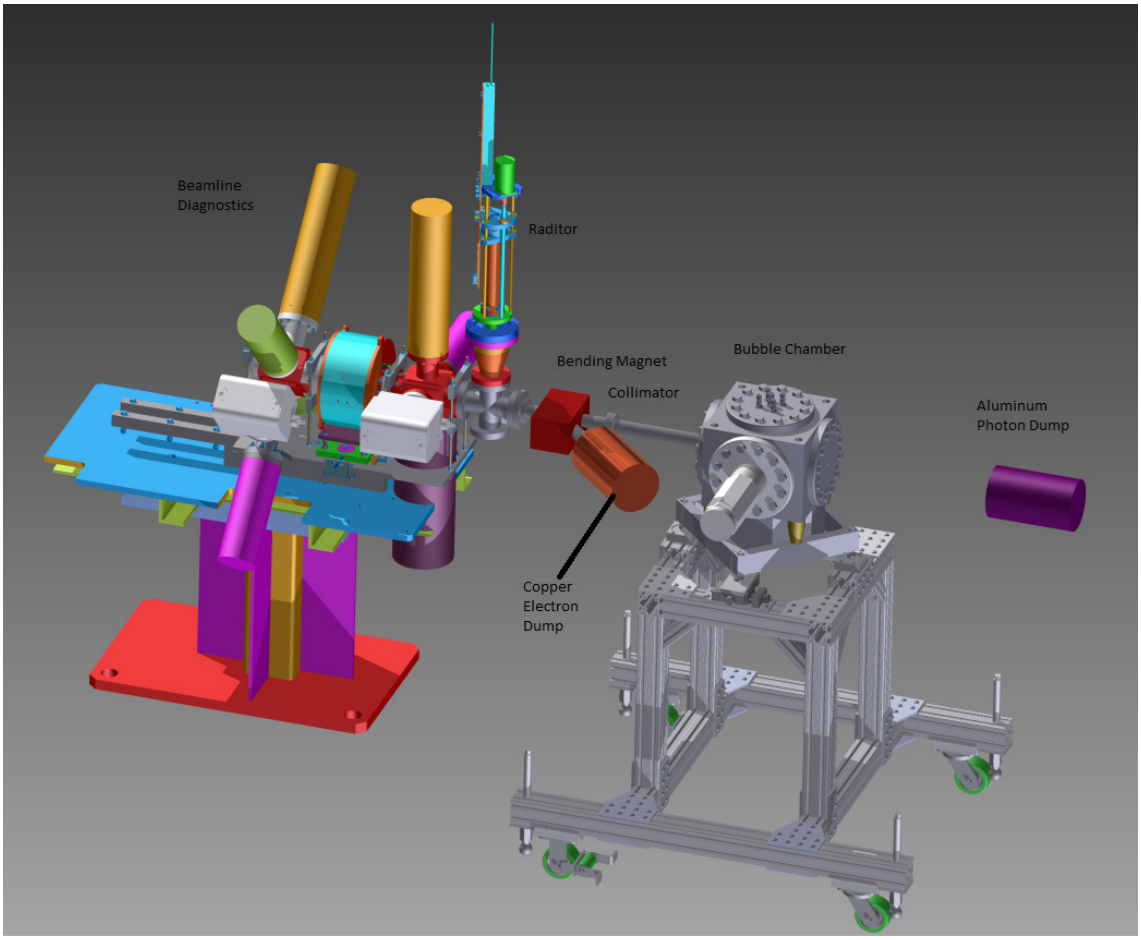

Fig. 12. Schematic of the proposed experiment.

The photon yield that hits the bubble chamber is shown in figure 14. Here the electron beam has a kinetic energy of 8.5 MeV and is irradiating the 0.02 mm Cu radiator. Since the $^{16}O(\gamma,\alpha)^{12}C$ cross section is very steep, only photons next to the end point will produce events from this reaction.

6.1 Systematic errors

The uncertainty in the absolute beam energy will be the dominant systematic error. There are a few improvements to the current setup that can help reduce this uncertainty, such as using a dipole with a better magnetic field uniformity and an accurate and more stable 10 A magnet power supply. The PEPPo collaboration is now doing a very careful analysis of

Beam Energy, E (MeV)	3.0 – 8.5
Beam Current (μA)	0.01-100
Absolute Beam Energy	1.0%
Relative Beam Energy	0.1%
Energy Resolution (Spread)	0.4%
Beam Size,$\sigma_{x,y}$ (mm)	0.3

Fig. 13. Electron beam properties used to produce the bremsstrahlung beam.

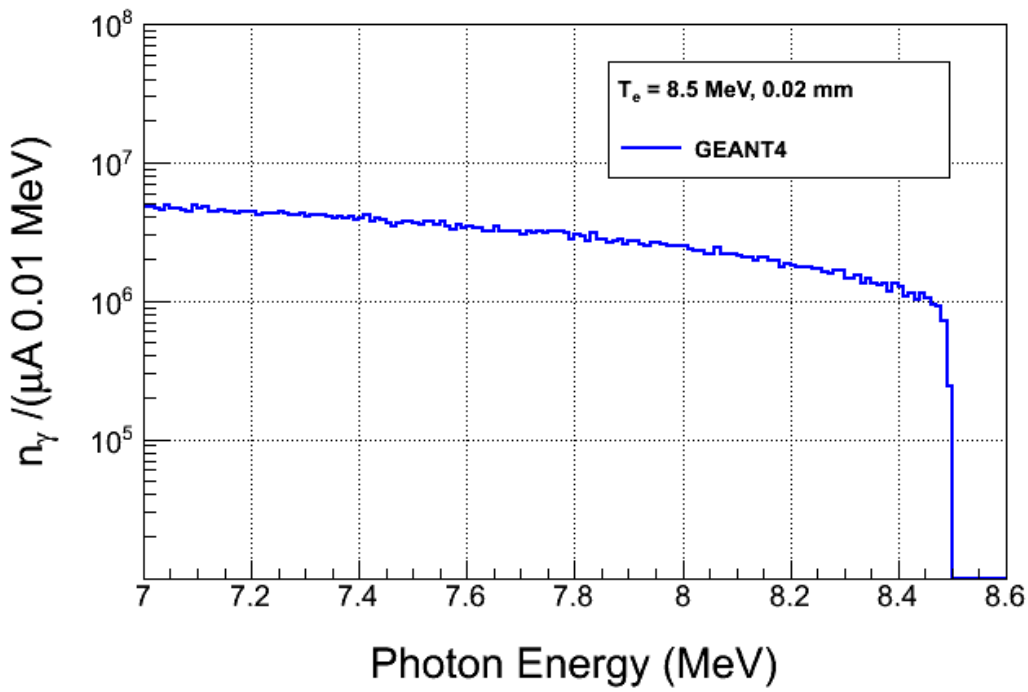

Fig. 14. GEANT4 simulation of the bremsstrahlung beam produced by an electron beam with kinteic energy of 8.5 MeV hitting a 0.02 mm Cu radiator.

the beam energy in the injector and will provide a list of the uncertainties that contribute to the overall error in the absolute beam energy. We will come up with means to reduce the dominant uncertainties to achieve the best measurement of the beam energy. We expect to reduce the uncertainty on the absolute beam energy determination by a factor of 5. Table 2 lists the cross section relative systematic error due to a 0.2% energy error.

The photon flux will be calculated using GEANT4. GEANT4 was shown to be capable of calculation of photon flux to 5% [34]. The thickness of both the radiator and the target will contribute an additional 3% each. The systematic error budget is shown below in table 1.

6.2 Beam time request and summary

Table 3 shows the beam requirement to measure the cross section at 7 different energies. The maxiumum avaliable energy in the injector is 8.5 MeV limited by field emission in the 1/4 cryomodule.

Table 4 gives the expected total number of $^{16}O(\gamma,\alpha)^{12}C$ events. The statistical error is about 4%. The parameters used in the calculation are: N_2O density = 0.846 g/cm^3, bubble chamber length = 3.0 cm, and radiator thickness = 0.02 mm.

To extract the cross section for the expected yield, we used GEANT4 and the Penfold-Leiss method [35]. In the past, the Penfold-Liess technique has produced unreliable results due to the low statistics used. Through Monte Carlo simulations, we have demonstrated that these problems can be overcome (see discussion in Appendix A).

The unfolded cross sections with their expected statistical errors are listed in table 5 and shown in Fig. 15. An estimate of the projected S-factor error bars is given in figure 16.

A total of (170 + 14) hours of beam time is needed to measure the $^{16}O(\gamma,\alpha)^{12}C$ cross section. The time budget comprises 170 hours of beam time (100% effciency of experiment and accelerator beam-on-target time) for the measurements, plus two hours per energy change for beam tuning.

As the bubble chamber will be exposed to a bremsstrahlung beam for the first time, an additional 152 hours of beam time will be required to commission the device. Here we will study the detector response to changes in the beam parameters and verify that background rates are similar to the expected values. In total, this amounts to 336 hours (or two weeks) of beam time.

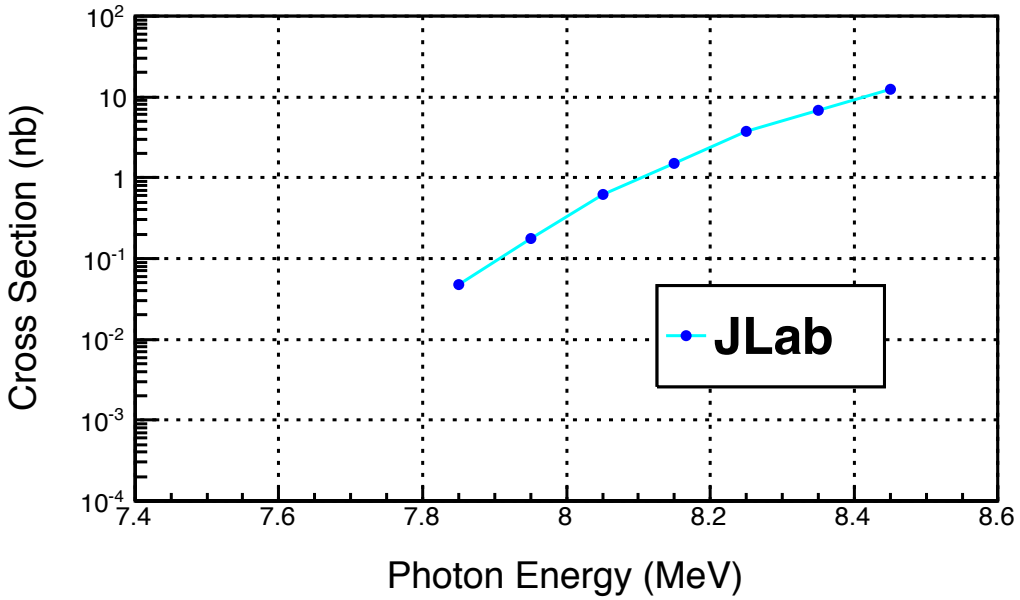

Fig. 15. Unfolded cross sections.

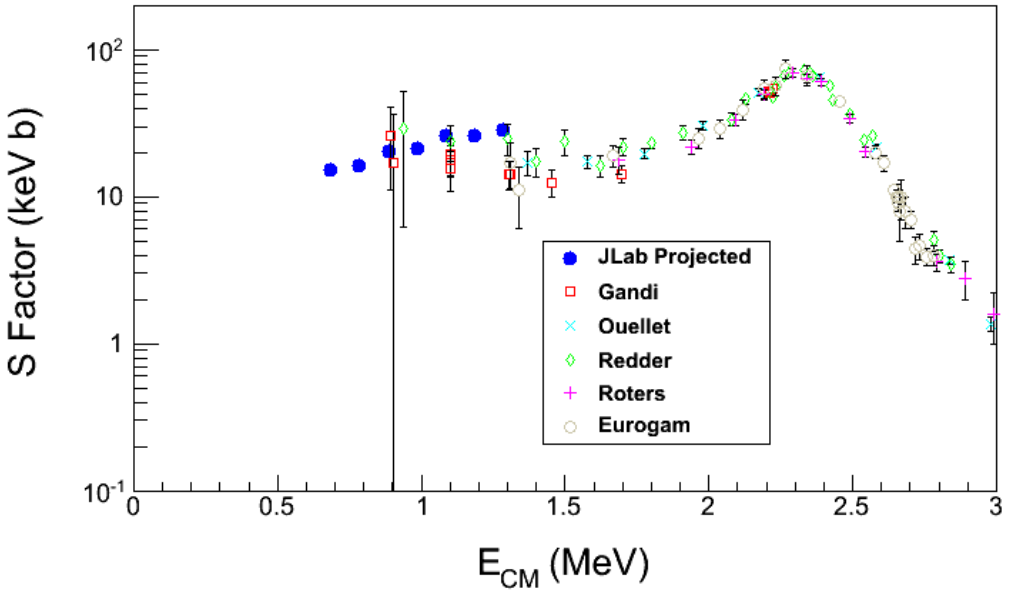

Fig. 16. Projection of S-factor error bars. The error bars only include statistical contributions.

References

[1] E. E. Salpeter. Nuclear Reactions in Stars Without Hydrogen. Astroph. J., 115:326–328, March 1952.

[2] C. W. Cook, W. A. Fowler, C. C. Lauritsen, and T. Lauritsen. B^{12}, C^{12}, and the Red Giants. Phys. Rev., 107:508–515, Jul 1957.

[3] C. Tur, A. Heger, and S. M. Austin. Dependence of s-process nucleosynthesis in massive stars on triple-alpha and ^{12}C(α,γ)^{16}O reaction rate uncertainties. Astroph. J., 702(2):1068, 2009.

[4] Philipp Podsiadlowski. Supernovae and gamma ray bursts. Springer, 2013.

[5] Wolfgang Hillebrandt and Jens C. Niemeyer. Type Ia Supernova explosion models. Ann. Rev. Astron. Astrophys., 38(1):191–230, 2000.

[6] Inma Dominguez, Peter Hoflich, and Oscar Straniero. Constraints on the progenitors of type ia supernovae and implications for the cosmological equation of state. Astroph. J., 557(1):279, 2001.

[7] R. E. Azuma, L. Buchmann, F. C. Barker, C. A. Barnes, J. M. D'Auria, M. Dombsky, U. Giesen, K. P. Jackson, J. D. King, R. G. Korteling, P. McNeely, J. Powell, G. Roy, J. Vincent, T. R. Wang, S. S. M. Wong, and P. R. Wrean. Constraints on the low-energy $E1$ cross section of ^{12}C(α,γ)^{16}O from the β-delayed α spectrum of ^{16}N. Phys. Rev. C, 50:1194–1215, Aug 1994.

[8] S.E. Koonin, T.A. Tombrello, and G. Fox. A hybrid r-matrix-optical model parametrization of the 12c(a,g)16o cross section. Nucl. Phys. A, 220(2):221 – 232, 1974.

[9] F. C. Barker and T. Kajino. The 12c(a,g)16o cross section at low energies. Aust. J. Phys., 44:369, 1991.

[10] B. W. Filippone, J. Humblet, and K. Langanke. K -matrix analysis of the ^{12}C(α , γ) reaction at low energy. Phys. Rev. C, 40:515–524, Aug 1989.

[11] C. R. Brune. Alternative parametrization of R-matrix theory. Phys. Rev. C, 66:044611, 2002.

[12] R. Plaga, H.W. Becker, A. Redder, C. Rolfs, H.P. Trautvetter, and K. Langanke. The scattering of alpha particles from 12c and the 12c(a,g)16o stellar reaction rate. Nucl. Phys. A, 465(2):291 – 316, 1987.

[13] C. Angulo and P Descouvemont. R-matrix analysis of interference effects in $^{12}C(\alpha,\alpha)^{12}C$ and $^{12}C(\alpha,\gamma)^{16}O$. Phys. Rev. C, 61:064611, 2000.

[14] P. Tischhauser, R. E. Azuma, L. Buchmann, R. Detwiler, U. Giesen, J. Görres, M. Heil, J. Hinnefeld, F. Käppeler, J. J. Kolata, H. Schatz, A. Shotter, E. Stech, S. Vouzoukas, and M. Wiescher. Elastic α-^{12}c scattering and the ^{12}C(α,γ)^{16}O E2 S-factor. Phys. Rev. Lett., 88:072501, Jan 2002.

[15] C.R. Brune, J. Daly, R. Detwiler, B. Fisher, W.H. Geist, J. Grres, H.J. Karwowski, R.W. Kavanagh, D.S. Leonard, P. Tischhauser, K.D. Veal, and M. Wiescher. Using sub-coulomb transfer reactions to study the low-energy 12c(a,g)16o s-factor. Nucl. Phys. A, 688(1-2):263 – 266, 2001. Nuclei in the Cosmos.

[16] L. Buchmann, R. E. Azuma, C. A. Barnes, J. M. D'Auria, M. Dombsky, U. Giesen, K. P. Jackson, J. D. King, R. G. Korteling, P. McNeely, J. Powell, G. Roy, J. Vincent, T. R. Wang, S. S. M. Wong, and P. R. Wrean. β-delayed α spectrum of ^{16}N and the ^{12}C(α,γ)^{16}o cross section at low energies. Phys. Rev. Lett., 70:726–729, Feb 1993.

[17] X. D. Tang, K. E. Rehm, I. Ahmad, C. R. Brune, A. Champagne, J. P. Greene, A. A. Hecht, D. Henderson, R. V. F. Janssens, C. L. Jiang, L. Jisonna, D. Kahl, E. F. Moore, M. Notani, R. C. Pardo, N. Patel, M. Paul, G. Savard, J. P. Schiffer, R. E. Segel, S. Sinha, B. Shumard, and A. H. Wuosmaa. New determination of the astrophysical S factor S_{E1} of the ^{12}C(α,γ)^{16}O reaction. Phys. Rev. Lett., 99:052502, Aug 2007.

[18] D. A. Glaser. Some effects of ionizing radiation on the formation of bubbles in liquids. Phys. Rev., 87:665, 1952.

[19] F. Seitz. On the theory of the bubble chamber. Phys. Fluids, 1:2, 1958.

[20] W. J. Bolte *et al*. Developmemt of bubble chambers with enhanced stability and sensitivity to low energy nuclear recoils. Nucl. Instr. and Meth. A, 577:569–573, 2007.

[21] M. J. Harper. Calculation of recoil ion effective track lengths in neutron-radiation-induced nucleation. Nucl. Sci. Eng., 114:118–123, 1993.

[22] J. F. Ziegler, J. P. Biersack, and U. Littmark. The Stopping and Range of Ions in Solids. Pergamon Press, 2009.

[23] C. R. Bell. Radiation Induced Nucleation of the vapor phase. PhD thesis, MIT, 1965.

[24] V. Zacek. Search for dark matter with moderately superheated liquids. Nuovo Cimento A, 107:291–298, 1994.

[25] G. Riepe and B. Hahn. Untersuchungen zum mechanismus del blasenbildung in freon-12 und propan durch ruckstosskerne einiger alpha strahler. Helv. Phys. Acta, 34:865, 1961.

[26] C. Matei, L. Buchmann, W. R. Hannes, D. A. Hutcheon, C. Ruiz, C. R. Brune, J. Caggiano, A. A. Chen, J. D'Auria, A. Laird, M. Lamey, ZH. Li, WP. Liu, A. Olin, D. Ottewell, J. Pearson, G. Ruprecht, M. Trinczek, C. Vockenhuber, and C. Wrede. Measurement of the cascade transition via the first excited state of ^{16}O in the ^{12}C(α,γ)^{16}O reaction, and its s factor in stellar helium burning. Phys. Rev. Lett., 97:242503, Dec 2006.

[27] D. Schurmann, L. Gialanella, Kunz. R., and F. Strieder. The astrophysical S-factor of ^{12}C(α,γ)^{16}O at stellar energy. Phys. Lett. B, 711:35–40, 2012.

[28] D. A. Glaser. Elementary Particles and Bubble Chambers. Elsevier Publishing Company, Amsterdam, 1964.

[29] C. Ugalde, B. DiGiovine, D. Henderson, R. J. Holt, K. E. Rehm, A. Robinson, A. Sonnenschein, G. Rusev R. Raut, and A. P. Tonchev. Bubble chambers as devices for measuring astrophysical thermonuclear rates. Phys. Lett. B, 719:74, 2013.

[30] H. R. Weller *et al*. Research opportunities at the upgraded HIγS facility. Prog. Part. Nucl. Phys., 62:257, 2009.

[31] S. Carson *et al*. Ratio of germanium detector peak efficiencies at photon energies of 4.4 and 11.7 mev: Experiment versus simulation. Nucl. Instr. and Meth. A, 618(1-3):190 – 198, 2010.

[32] S. Wilmes, V. Wilmes, G. Staudt, P. Mohr, and J.W. Hammer. The $^{15}N(\alpha,\gamma)^{19}F$ reaction and nucleosynthesis of ^{19}F. Phys. Rev. C, 66:065802, 2002.

[33] F. Aubin *et al*. Discrimination of nuclear recoils from alpha particles with superheated liquids. New J. Phys., 10:103117, 2008.

[34] B. A. Faddegon, M. Asai, J. Perl, C. Ross, J. Sempau, J. Tinslay, and F. Salvat. Benchmarking of monte carlo simulation of bremsstrahlung from thick targets at radiotherapy energies. Med. Phys., 35:4308, 2008.

[35] A. S. Penfold and J. E. Leiss. Analysis of photonuclear cross sections. Phys. Rev., 114:1332, 1959.

[36] R.E. Sund *et al.* $^{141}Pr(\gamma,n)$ cross section from threshold to 24 mev. Phys. Rev. C, 2:1129, 1970.

[37] L. I. Schiff. Energy-angle distribution of thin target bremsstrahlung. Phys. Rev., 83:252, 1951.

[38] D. J. S. Findlay. A modification to the Penfold-Leiss method of cross section unfolding. Nucl. Instr. and Meth., 213:353, 1983.

[39] D. J. S. Findlay *et al.* Photofission of ^{232}Th near threshold. Nucl. Phys. A, 458:217, 1986.

[40] S. J. Watson *et al.* Photofission and photoneutron measurements on ^{241}Am between 5 and 10 mev. Nucl. Phys. A, 548:365, 1992.

7 Appendix A

When using Bremsstrahlung photon beam to study photo-nuclear reactions, the yield (number of reactions) is given by:

$$y(E) = \int_{Threshold}^{E} N_\gamma(E,k)\sigma(k)dk \tag{5}$$

where E is the electron beam kinetic energy, $N_\gamma(E,k)$ is the number of gammas per energy unit which depends on the electron energy and the gamma energy. The continuous range of photon energies means that the cross section is not measured directly, instead it must be unfolded from the measured yields.

An integral equation of this form is known as Volterra Integral Equation of the first kind. $\sigma(k)$ is the function to be solved for. One way to solve the yield integral equation is to use the Method of Quadratures (a method for constructing an approximate solution of an integral equation based on the replacement of integrals by finite sums). First the yields measured at $E = E_1, E_2, \ldots, E_n$ where $E_i - E_{i-1} = \Delta$, $i = 2, \ldots, n$. Then,

$$y(E_i) = \int_{Threshold}^{E_i} N_\gamma(E_i,k)\sigma(k)dk \approx \sum_{j=1}^{i} N_\gamma(E_i,\Delta,k_j)\sigma(k_j) \tag{6}$$

Where $N_\gamma(E_i,\Delta,k_j)$ is the number of gammas in the energy bin of width Δ.

Equation 6 is a set of linear equations which can be written in the matrix form:

$$\begin{pmatrix} y_1 \\ y_2 \\ \vdots \\ y_n \end{pmatrix} = \begin{pmatrix} N_{11} & N_{12} & \cdots & N_{1n} \\ N_{21} & N_{22} & \cdots & N_{2n} \\ \vdots & \vdots & \ddots & \vdots \\ N_{n1} & N_{n2} & \cdots & N_{nn} \end{pmatrix} \begin{pmatrix} \sigma_1 \\ \sigma_2 \\ \vdots \\ \sigma_n \end{pmatrix} \tag{7}$$

This matrix equation can be solved with matrix inversion.

Equivalently, the solution to Equation 6 can be written:

$$\sigma_i = \frac{1}{N_{ii}}\left[y_i - \sum_{j=1}^{i-1}(N_{ij}\sigma_j)\right] \tag{8}$$

The error propagation of Equation 8 is given by:

$$\left(\frac{d\sigma_i}{\sigma_i}\right)^2 = \frac{\left[(dy_i)^2 + \sum_{j=1}^{i-1}(N_{ij}d\sigma_j)^2\right]}{\left[y_i^2 - \sum_{j=1}^{i-1}(N_{ij}\sigma_j)\right]^2} \tag{9}$$

For mono-chromatic photon beam, Equation 9 reduces to:

$$\left(\frac{d\sigma_i}{\sigma_i}\right)^2 = \left(\frac{dy_i}{y_i}\right)^2 = \frac{1}{y_i}. \tag{10}$$

Initially, the above unfolding method known as Penfold-Liess unfolding [35] gave unreliable results (see for example [36]) because (in the sixties and seventies) the unfolding procedures have been often considered in isolation from the photon energy spectrum of the bremsstrahlung beam used experimentally. At that time, experimentalists used the Schiff theoretical formula [37] to calculate $N_{ij} = N(E_i, k_j - \Delta/2)$. Findlay proposed [38] that a simple modification to Nij prevents the generation of spurious results. He replaced $k - \Delta/2$ by $k - \lambda\Delta$ where λ is a parameter determined by considering the energy spread of the electron beam and the energy loss of the electron beam in the radiator. Findlay's modification was successfully demonstrated in [39,40].

These days, there are very accurate Monte-Carlo simulations, N_{ij} can be calculated for each specific experimental conditions without the need to use theoretical formula. This removes problems in the unfolding related to the knowledge of N_{ij}.

However, this is not the only reason that may cause Penfold-Liess unfolding to fail. Careful inspection of Equation 9 reveals that statistical errors of the measured yield play a role in two ways. First, the statistical errors add up as can be seen in the numerator of the right hand side of Equation 9. Although σ_1 and probably σ_2 will be very closed to their real values, the remaining cross section data points will start to oscillate. Second, the denominator of the difference of two large numbers and thus will enhance the error in the cross section since the difference will be a smaller number. Indeed, having a very steep cross section is an advantage here, since it reduces the second term in the denominator and give a denominator with large number. To determine the required statistical error for each yield measurement, the steepness of the cross section must be taken into account. A relatively flat cross section requires very accurate yield measurement to be able to successfully unfold the cross section.

Luckily for us, our cross section is very steep and only photons near the endpoint contribute to the yield for each beam energy. Similar arguments show that is is beneficial to maximize

the number of gammas near the endpoint relative to the number of gammas at lower gamma energy, N_{ii}/N_{ij}, $j = 1, \ldots, i-1$. This is one reason, among many others, why we chose to run with a very thin Bremsstrahlung radiator.